applied mechanics

Article

A Crystal Plasticity-Based Simulation to Predict Fracture Initiation Toughness of Reactor-Grade Aluminium: Experimental Verification and Study of Effect of Crystal Orientation

Mahendra Kumar Samal [1,2,*], Trishant Sahu [3] and Ather Syed [2]

[1] Division of Engineering Sciences, Homi Bhabha National Institute (HBNI), Mumbai 400094, India
[2] Reactor Safety Division, Bhabha Atomic Research Centre, Mumbai 400085, India; ather@barc.gov.in
[3] Reactor Operations Division, Bhabha Atomic Research Centre, Mumbai 400085, India; trishant@barc.gov.in
* Correspondence: mksamal@barc.gov.in; Tel.: +91-22-2559-3551

Abstract: Aluminium alloys are used for the fabrication of the fuel clad of research-grade nuclear reactors as well as for several types of core components of high-flux research reactors. In order to carry out design and safety analysis of these components, their mechanical and fracture properties are required by the designer. In this work, experiments have been conducted on tensile specimens machined from an aluminium alloy block to evaluate the material stress-strain curve. Experiments have also been conducted on disc-shaped compact tension specimens in order to determine the fracture toughness of aluminium alloy. Numerical simulations of both tensile and fracture specimens have been carried out using the crystal plasticity model. Initially, the slip system level parameters of the crystal plasticity material model have been calibrated using experimental stress-strain data for single as well as polycrystalline aluminium. For the prediction of crack initiation toughness, Rice and Tracey's damage model has been used. The critical damage parameter has been evaluated for a fractured specimen with a crack length-to-width (a/W) ratio of 0.6. The attainment of the critical damage parameter in the analysis corresponds to the instance of experimentally observed ductile crack initiation in the specimen. Later, this model was applied to other fracture specimens with different a/W ratios with values ranging from 0.39 to 0.59. It was observed that the critical damage parameter corresponding to crack initiation in the material has a very small variation, even if the specimens have different crack lengths. It is well-known in the literature that Rice and Tracey's critical damage parameter is a material constant. Hence, we have applied the same model to predict crack initiation for single crystal fracture specimens with two different orientations of the crack plane. It was observed that the <111> orientation is more susceptible to crack initiation and propagation compared with the <100> orientation, as the damage parameter is high in the ligament of the specimen ahead of the crack tip for the same level of applied loading. As the [111] crack plane is more closely packed compared with the [100] plane, the distance between atomic planes is greater for the former, and hence, it is more susceptible to ductile damage. The results of the experiments and the material damage parameter are helpful for the integrity analysis of the fuel clad of research reactors as well as components of high-flux research reactors.

Keywords: fracture initiation toughness; J-resistance curve; aluminium; damage parameter; crystal orientation; crystal plasticity; disc-shaped specimen; fracture test; Rice and Tracey's model

check for updates

Citation: Samal, M.K.; Sahu, T.; Syed, A. A Crystal Plasticity-Based Simulation to Predict Fracture Initiation Toughness of Reactor-Grade Aluminium: Experimental Verification and Study of Effect of Crystal Orientation. *Appl. Mech.* **2024**, *5*, 513–532. https://doi.org/10.3390/applmech5030029

Received: 15 May 2024
Revised: 3 July 2024
Accepted: 12 July 2024
Published: 17 July 2024

1. Introduction

The fracture process is a complex physical phenomenon that spans various length scales ranging from atomistic to continuum scale. The fracture process is called brittle if it occurs with little or negligible plastic deformation [1]. On the other hand, the ductile fracture process is associated with plastic deformation at the crack tip. Crack initiation and growth in fracture specimens occur due to the mechanism of nucleation, growth,

and coalescence of voids with the existing crack tip [2]. This fracture initiation process is affected by the presence of micro-defects like second-phase particles, which act as sites for nucleation of micro-voids. The microvoids may also form due to the process of decohesion of particles from the matrix, cracking of these particles, etc. [3].

An important alloy that is widely used in research-grade reactors is the aluminium alloy Al-1100. For safety and integrity analysis of reactor components made of this alloy, it is essential to understand the ductile crack initiation process in this material and evaluate a critical damage parameter so that the same can be used for integrity analysis of reactor components once its magnitude is evaluated from laboratory scale experiments. Understanding the ductile crack initiation process in aluminium alloys is important from the point of view of safety and integrity analysis of reactor components. On the other hand, the evaluation of a critical damage parameter for the alloy Al-1100 shall help in predicting the fracture initiation toughness of reactor components. Various types of aluminium alloys have been studied in the literature [4–12], and the earlier research work involves experimental and numerical simulations in order to evaluate the tensile and fracture properties of these alloys [4–12]. These researchers [4–12] present results on tensile and fracture properties of different grades of aluminium alloy and discuss the details of experimental and numerical simulation approaches followed in their work.

The tensile and fracture behaviour of Al 6061 alloy was evaluated in refs. [4,5] The extended finite element method (XFEM) was used for the simulation of the tests [4,5]. XFEM was also used to simulate ductile crack propagation in ultrafine-grained 7075 aluminium alloy in ref. [6] The ductile crack growth in tensile specimens of aluminium was studied experimentally in ref. [7] The fracture toughness was evaluated using notched bars of aluminium 6061-T6 by Hellier et al. [8] The tensile properties and fracture toughness data of Al–Li 8090 alloys were evaluated and correlated with microstructural features in ref. [9] The plane stress fracture toughness for ultra-fine grained aluminium thin sheet was evaluated in ref. [10] and the mode-I fracture toughness of different types of aluminium alloys was evaluated in refs. [11–15].

The high-temperature deformation behaviour of extruded Al-7075 alloy was studied by Ye et al. [16] and Zhu et al. [17] The evolution of texture of this material during the process of hot deformation was studied using the visco-plastic self-consistent model [17]. The mechanical properties of aluminium alloy parts fabricated by the laser powder bed fusion process were correlated to the microstructure in ref. [18] The influence of forming orientation and loading rate on the shear deformation behaviour of aluminium alloy was studied in ref. [19] Various other studies [20–27] have focussed on enhancing the strength and toughness of aluminium alloys through different methods of heat treatment (such as aging), cryo-rolling, use of machine learning to optimise the process, friction stir processing, post-weld heat treatment, etc.

The concept of work of fracture has been used to simulate crack initiation and propagation in aluminium alloys in ref. [28] and cohesive zone method has been used to simulate crack growth in thin aluminium sheets in ref. [29] In order to understand the crack initiation process in aluminium alloys, it is imperative to quantitatively analyse crack tip stress and strain fields. Several investigators have investigated the crack tip stress and strain fields for single crystal as well as polycrystalline materials [30–36]. Rice [31] proposed an asymptotic solution for the crack tip stress field in ductile single crystals subjected to mode I plane strain loading conditions within the framework of small strain formulation and assuming the material to be perfectly plastic. The analysis presented in ref. [31] considered the case of a crack on the [010] plane with a crack front along the $< 10\bar{1} >$ direction and another crack on the {101} plane with a crack front along the $< 10\bar{1} >$ direction. Both face-centred-cubic (FCC) and body-centred-cubic (BCC) crystals were considered in the analysis. The above study conducted with varying orientations and lattice types showed that the crack tip fields in a single crystal are influenced by grain orientation as well as the type of crystal lattice [31].

Similar studies in atomistic scale were carried out by various researchers [32,33], specifically to analyse the stress evolution ahead of the crack tip. The other objective of these works was to study the effect of void size and distance of void from a crack tip on the fracture response of FCC single crystal. In crack tip stress field evolution studies presented in the literature [32,33], a constrained 3D atomic model of aluminium was used to evaluate the crack tip field in terms of von Mises stress, mean stress and stress triaxiality. The effect of void nucleation, crack initiation and propagation on the crack tip stress field was also studied.

In ref. [32], simulations were carried out with aluminium single crystal-loaded at a strain rate of $10^8 s^{-1}$ in the <010> direction. Results of crack tip stress and strain fields, crack tip constraints, the influence of crack tip constraint on void growth, and interaction between a notch and cylindrical voids in single crystals were presented in detail in ref. [33–36] For the simulation of ductile crack initiation using continuum scale methods, Rice and Tracey's ductile damage model [30] is widely used in the research literature [37,38]. The model has also been used in crystal plasticity simulations to predict fatigue crack initiation in Titanium alloys in ref. [38].

From a thorough literature survey, it was found that research work on the evaluation of tensile and fracture properties of aluminium alloy Al-1100 is very scarce in the open literature. Hence, the purpose of this work is to evaluate the above-mentioned properties of a reactor-grade aluminium alloy experimentally. In addition, crystal plasticity simulations have been carried out for single and polycrystalline specimens to evaluate the stress and strain field ahead of the crack tip of a standard disc-shaped fracture specimen. The value of the critical damage parameter to predict ductile crack initiation as per the Rice and Tracey model [30] has also been evaluated.

Initially, experiments are conducted on tensile specimens machined from an aluminium alloy block to evaluate the material stress-strain curve. Later, experiments were conducted on disc-shaped compact tension (DCT) specimens in order to determine the fracture toughness of aluminium alloy. The variation of the critical damage parameter for various values of initial crack length-to-width (a/W) ratios of the disc-shaped CT specimens has been studied. In addition, the critical material damage parameter has also been used to study the crack initiation in single crystal fracture specimens with two different orientations (i.e., [100] and [111]) of the crack plane.

2. Material Composition and Mechanical Properties

The material used in this work is aluminium and it is of grade Al-1100-O (O refers to annealed or without cold-work). The alloy is of nuclear reactor-grade of pure aluminium. The chemical composition of aluminium alloy Al-1100-O is given in Table 1. This is the commercial grade of pure aluminium with almost 99–99.5% Al, and the rest are trace elements. Among the trace elements, Fe and Si constitute the major fraction, followed by Zn, Mn, and Cu. The alloy is not heat-treatable, and hence, the strength arises mainly because of the Al matrix with a very small fraction of second-phase particles and inclusions.

Table 1. Chemical composition of aluminium used for tests in this work.

Element	Cu	Mn	Fe + Si	Zn	Al
Wt.%	0.05–0.2	0.05 (max)	0.95 (max)	0.1 (max)	99–99.95

The mechanical properties of this alloy have been evaluated through tensile tests of flat-type specimens. The mechanical properties of the alloy at 25 °C (room temperature), as evaluated from the tensile test, are given in Table 2.

Table 2. Mechanical properties of aluminium used for tests in this work at 25 °C.

Mechanical Property	Young's Modulus (GPa)	Poisson's Ratio	Yield Strength (MPa)	Ultimate Tensile Strength (MPa)	Uniform Elongation (%)	Ductility (%)
Value	70	0.33	32	75	10	23

3. Fracture Experiments Using Disc-Shaped Compact Tension Specimen

For evaluating fracture resistance data of aluminium alloy, disc-shaped specimens of 41 mm diameter and 3 mm thickness were machined from cylindrical blocks of aluminium alloy (which are usually used for the fabrication of the fuel clad of research reactors). The geometrical dimensions of the specimens are shown in Figure 1. The specimen is loaded through fixtures for the fracture tests, and a photograph of the test setup is shown in Figure 2.

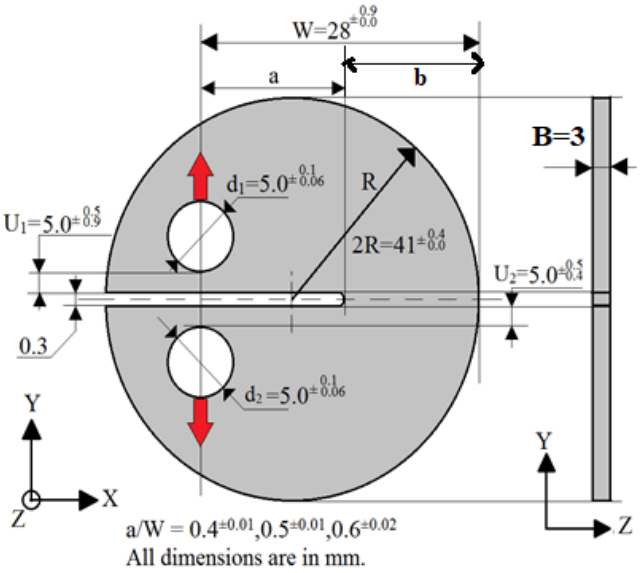

Figure 1. Geometrical details of the disc-shaped compact tension fracture specimen used in the test.

(**a**) (**b**)

Figure 2. (**a**) picture of test setup to carry out fracture tests on disc-shaped compact tension fracture specimen, (**b**) fixtures and the specimen loaded in the test setup.

The exact dimensional details of the nine different disc-shaped specimens are provided in Table 3. These data have been obtained by carrying out dimensional measurements on the specimens after their fabrication. The load-displacement data for all nine specimens with different a/W ratios (nominal values of 0.4, 0.5 and 0.6), as obtained from the experiments, are shown in Figure 3.

Table 3. Dimensional details of all disc-shaped CT specimens used in the test (symbols are as per Figure 1).

Nominal a/W	Specimen No.	a/W (Measured)	W	b	B	2R	U_1	U_2	d_1	d_2
			(mm)							
0.6	1	0.586	29.06	12.03	2.8	41.26	4.45	4.75	4.97	4.94
	4	0.58	28.09	11.79	2.9	41.26	4.46	5.39	5.02	5
	7	0.586	28.79	11.9	3.1	41.24	5.04	4.92	5.01	5
0.5	2	0.496	28.95	14.59	2.96	41.23	4.98	5.08	4.47	4.45
	5	0.494	28.65	14.48	2.8	41.1	5.1	4.6	5.03	5
	8	0.495	28.92	14.58	3	41.21	4.9	4.7	5.06	5.04
0.4	3	0.4	28.83	17.29	3	41.37	4.66	5.51	5.07	5.06
	6	0.389	28.43	17.36	3	41.29	4.1	5	5.01	5.09
	9	0.394	28.88	17.5	2.98	41.36	4.2	5.3	4.93	5.03

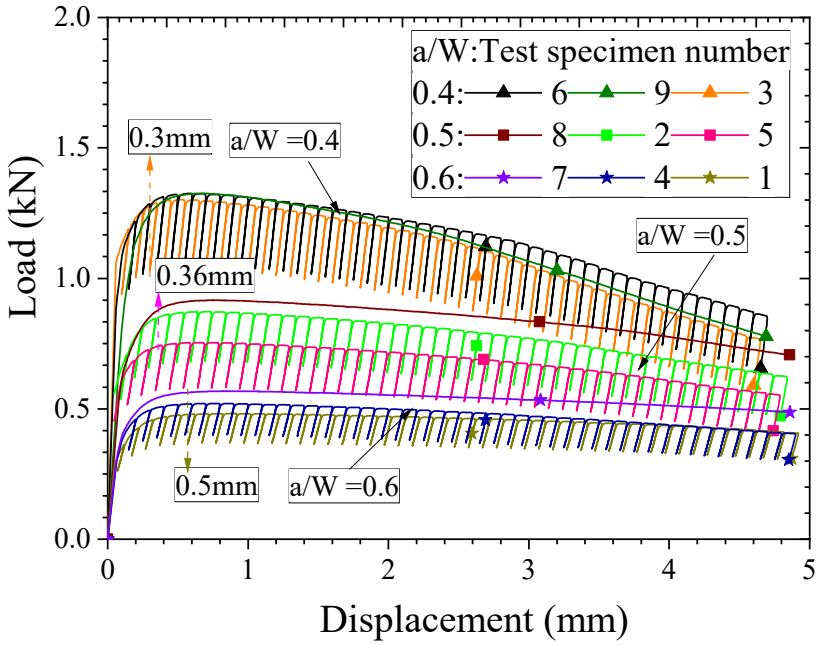

Figure 3. Load-displacement data of all the nine specimens with different a/W ratios as obtained from experiments.

The repeated tests with nominal a/W ratios of 0.4, 0.5, and 0.6 are very close to each other for each set of specimens with similar a/W ratios except for test No. 5 (with $a/W = 0.5$). It can be seen from Figure 3 that the load-carrying capability of the specimens increases with a decrease in the a/W ratio. As the a/W ratio decreases, the remaining ligament (b) becomes more, and hence, the load-carrying capacity of the specimen increases. However, the fracture resistance depends upon the plastic deformation energy rate associated with ductile crack growth (i.e., the plastic area under the load-displacement curve per unit area of crack extension) as well as on the rate of crack growth. As crack growth changes with

applied displacement, information on both the parameters (i.e., the area under the load-displacement curve and crack growth rate) is required to evaluate the fracture resistance curve. The standard ASTM E1820 [39] elaborates the method to calculate crack initiation toughness and *J-R* curve while using a fracture specimen and the same has been followed here. The details of the scheme for the evaluation of fracture toughness data are presented in the following paragraphs. The photographs of the specimens after the tests are shown in Figure 4. The final crack growth data was measured directly from the specimens after the completion of the test.

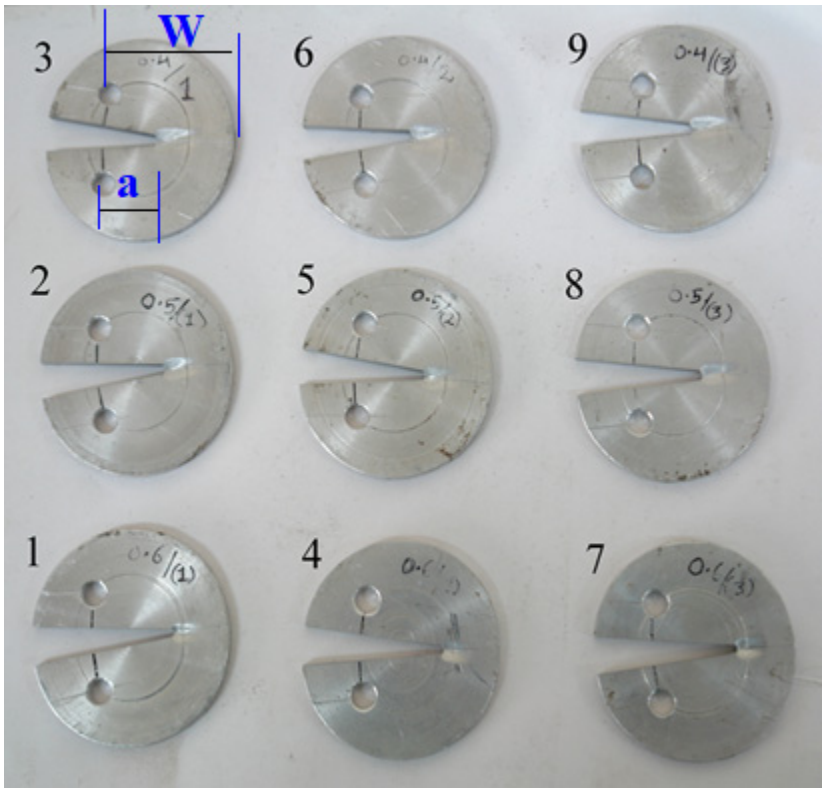

Figure 4. Photographs of nine disc-shaped compact tension fracture specimens with different a/W ratios after the test (specimen numbers are as per Table 3).

The crack growth in the specimens during the test has been measured using the unloading compliance technique [39]. This method requires the evaluation of compliance data of the specimen during the test (as crack length changes continuously). The same is evaluated from the unloading slopes of load-displacement curves, as presented in Figure 3. The load-line compliance of the specimen (C_{LL}) depends upon the crack length-to-width (a/W) ratio. The specimens with a larger crack length have more compliance and vice versa. For the disc-CT specimen, the correlation of specimen compliance with a/W ratio is given by Equation (1) [39].

$$C_{LL}(a/W) = \frac{1}{EB_e}\left(\frac{1+a/W}{1-a/W}\right)^2 \left[2.0462 + 9.6496(a/W) - 13.7346(a/W)^2 + 6.1748(a/W)^3\right] \quad (1)$$

where E is Young's modulus of elasticity, a is crack length, W is width, and B_e is the effective thickness of the specimen. For the specimen without a side groove, $B_e = B$, and for the specimen with a side groove and net thickness, B_N, $B_e = B - (B - B_N)^2/B$. In our case, B_e is the same as the actual thickness B. Using Equation (1), the value of a/W and, hence, crack length a is evaluated as a function of applied displacement for each specimen, and these data are presented in Figure 5. It was observed that crack growth is higher for the

specimen with a lower a/W ratio when compared with the other specimens with a higher a/W ratio for a given value of applied displacement. Specimen with a lower value of a/W ratio has a larger ligament ($b = W - a$) and more stiffness. Hence, for the same value of applied displacement (i.e., loading controlled loading), the crack growth becomes larger. For measuring crack initiation, a crack growth of 200 microns is usually considered in the literature [37,38]. Corresponding to these data of crack growth, the applied displacement values are evaluated as 0.3, 0.36, and 0.5 mm for specimens with nominal a/W ratios of 0.4, 0.5, and 0.6, respectively, as can be seen from Figure 5.

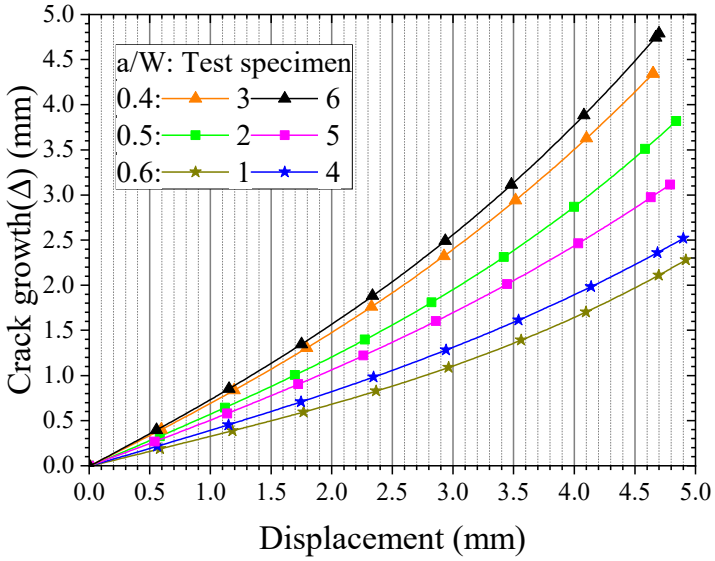

Figure 5. Crack growth vs. displacement data of disc-shaped compact tension specimens with different a/W ratios (0.4 to 0.6) as obtained from experiments.

The load-displacement data (Figure 3), along with the information on crack growth vs. applied displacement (Figure 5), are used to calculate the fracture resistance of the specimens in terms of the *J*-*R* or *J*-resistance curve. The method of calculation of the *J*-*R* curve for the disc-shaped CT is described in detail ref. [39] and it is provided here briefly. The J-resistance of the specimen increases with applied loading and it is calculated for each loading step using two components, i.e., J_{el} and J_{pl} (elastic and plastic part of *J*) as follows.

$$J = J_{el} + J_{pl} = K^2\left(1 - \nu^2\right)/E + J_{pl} \tag{2}$$

The elastic component is calculated using stress intensity factor '*K*' as presented in the first part of '*J*'. In Equation (2), '*E*' is Young's modulus of elasticity of the material and ν is Poisson's ratio. The stress intensity factor '*K*' is evaluated using load '*P*' and a geometric factor $f(a/W)$ as described in Equations (3) and (4), respectively. The dimensions B, B_N, and W are specimen thickness, net thickness (only in the presence of side groove), and width, respectively, and these are shown in Figures 1 and 4.

$$K = \frac{P}{\sqrt{BB_N W}} f(a/W) \tag{3}$$

$$\begin{aligned} f(a/W) \quad &= [1 - (a/W)]^{-1.5}\{(2 + a/W)\} \\ &\left[\begin{array}{l} 0.76 + 4.8(a/W) - 11.58(a/W)^2 \\ +11.43(a/W)^3 - 4.08(a/W)^4 \end{array}\right] \end{aligned} \tag{4}$$

The plastic part of '*J*' is evaluated in Equation (5) using the plastic area A_{pl} under the load-displacement curve (as presented in Figure 3) and two geometric factors, η and γ, as presented in Equation (6). The plastic area A_{pl} is evaluated by integrating the load-

displacement curve and subtracting the elastic energy from the total energy (i.e., the area under the load-displacement curve). The two geometric factors are again functions of a/W ratio and are presented in Equation (6).

$$J_{pl(i)} = \left[J_{pl(i-1)} + \frac{\eta}{Bb}\left(A_{pl(i)} - A_{pl(i-1)}\right)\right]\left[1 - \frac{\gamma}{b}(a_i - a_{i-1})\right] \quad (5)$$

$$\eta(a/W) = 2 + 0.522(1 - a/W);\ \gamma(a/W) = 1 + 0.76(1 - a/W) \quad (6)$$

The *J-R* curves of disc-shaped compact tension specimens (with different a/W ratios) as evaluated using ASTM E1820 standard procedure [39] are presented in Figure 6.

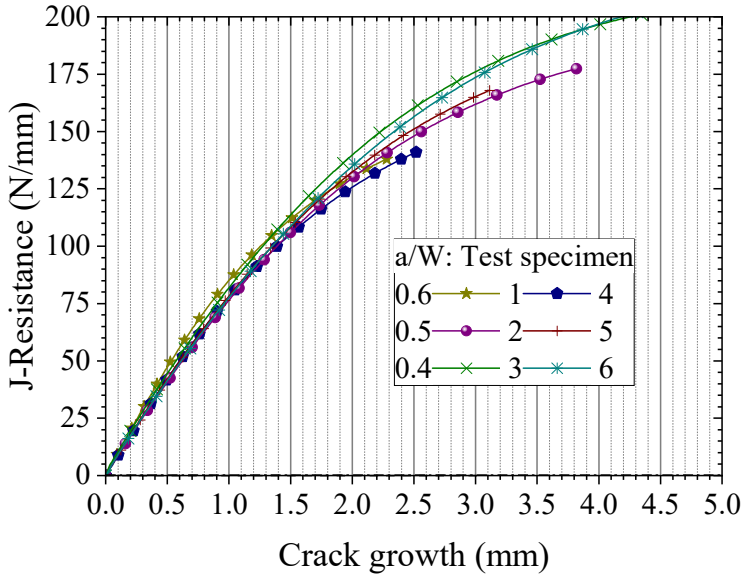

Figure 6. Fracture resistance (*J-R*) curves of disc-shaped compact tension specimens with different a/W ratios (0.4 to 0.6) as calculated from load-displacement and crack growth data.

It can be observed that the *J-R* curves of the specimens with a/W ratios varying from 0.4 to 0.6 are almost constant (i.e., they fall within a small experimental scatter band). These results are also consistent with ASTM E1820 specifications, where the initial a/W ratio of the specimen is recommended to lie in the range of 0.45 to 0.55.

4. Crystal Plasticity-Based Constitutive Model Used in the Numerical Simulation

Crystal plasticity simulations consider the material plastic deformation at the slip system level, where the deformation behaviour of single-crystal as well as polycrystalline materials can be predicted. In this work, the FE simulations are carried out using an in-house finite element-based code CRYSP [40,41]. The constitutive model employed in the in-house crystal plasticity code CRYSP is based on the formulation presented in the works of Balasubramanian and Anand [42] and Ma and Roters [43]. The model is presented in brief here for completeness. In the large strain formulation used in this work, the deformation gradient F is written as a product of elastic and plastic parts (i.e., F_e and F_P). The plastic velocity gradient L_p is calculated as a summation of the contribution of shear rates in each slip system (the contributions being the product of slip rate $\dot{\gamma}^{\alpha}$ in each slip system and Schmidt's tensor $m^{\alpha} \otimes n^{\alpha}$), i.e.,

$$L_p = \sum_{\alpha=1}^{n} \dot{\gamma}^{\alpha} m^{\alpha} \otimes n^{\alpha}. \quad (7)$$

The slip rate (in terms of shear strain rate) for the slip system α can be written in terms of the following equations, i.e., Equations (3)–(6). The details can be found in ref. [42–45].

$$\dot{\gamma}^{\alpha} = \begin{cases} 0 \text{ if } \tau_*^{\alpha} < s_*^{\alpha} \\ \gamma_0 \exp\left\{ \frac{-\Delta F_*}{k_b \theta} \left(1 - \left(\frac{\tau_*^{\alpha}}{s_*^{\alpha}} \right)^p \right)^q \right\} \mathrm{sgn}(\tau_*^{\alpha}) \end{cases} \tag{8}$$

$$\mathrm{h}^{\alpha\beta} = \underbrace{\left[(1 - q_1)\delta^{\alpha\beta} + q_1 \right]}_{\text{latent hardening}} \underbrace{h_0^{\beta} \left| 1 - \frac{s^{\beta}}{s_s^{\beta}} \right|^r \mathrm{sgn}\left(1 - \frac{s^{\beta}}{s_s^{\beta}} \right)}_{\text{self hardening } (h_{\beta})} \tag{9}$$

$$\dot{s}^{\beta} = (1 + \chi)\dot{s}_a^{\beta} \tag{10}$$

$$\dot{s}_a^{\alpha} = (1 + \chi)^{-1} \sum_{\beta} \mathrm{h}^{\alpha\beta} \left| \dot{\gamma}^{\beta} \right|; \; s_*^{\alpha} = \chi s_a^{\alpha} \tag{11}$$

In Equation (8), γ_0 is reference shear rate, ΔF_* is activation enthalpy for slip, k_B is Boltzman's constant, θ is the temperature in Kelvin scale, τ_*^{α} is resolved shear stress in slip system α, and s_*^{α} is the slip system resistance to dislocation motion and is given in Equation (11). The parameters 'p', 'q', and 'q_1' are material constants, and these are usually taken as 1.4, 1.1, and 0.6, respectively [42,43]. $h^{\alpha\beta}$ is the slip system hardening parameter, and it is a function of the slip system hardening constant h_0^{β}. The parameter s^{β} is self-hardening parameter for a slip system, s_s^{β} is the saturation magnitude of this parameter and χ is the cross-hardening parameter and the same is described in detail in ref. [43] After the plastic part of the velocity gradient is calculated, the rate of the plastic deformation gradient is calculated as follows.

$$\dot{F}_p = L_P F_P \tag{12}$$

Once the plastic part of the deformation gradient is updated, the elastic part is obtained from the total deformation gradient F, which is known at the start of the time step. The evaluation of the stress tensor through the stress update scheme and the evaluation of elastic and plastic parts of the strain tensor are carried out through standard procedures. The details of the same can be found in refs. [40–43] For the FCC materials like aluminium, there are 12 slip systems. The corresponding slip plane and slip directions are given by vectors, as shown in Table 4. These are used as inputs in the crystal plasticity simulation.

Table 4. Slip plane normal and slip directions for 12 slip systems of an FCC crystal like aluminium.

Slip Plane Normal n^{α}	Slip Direction m^{α}	α
$\{111\}$	$[1\bar{1}0]$	1
	$[\bar{1}01]$	2
	$[01\bar{1}]$	3
$\{\bar{1}11\}$	$[101]$	4
	$[\bar{1}\bar{1}0]$	5
	$[01\bar{1}]$	6
$\{1\bar{1}1\}$	$[\bar{1}01]$	7
	$[0\bar{1}\bar{1}]$	8
	$[110]$	9
$\{\bar{1}\bar{1}1\}$	$[\bar{1}10]$	10
	$[101]$	11
	$[0\bar{1}\bar{1}]$	12

5. Calibration of Parameters of the Crystal Plasticity-Based Constitutive Model for Single Crystals and Polycrystalline Aluminium

One of the important initial steps of crystal plasticity simulation is the calibration of slip system-level hardening parameters for a material. As the response of single crystals and polycrystals are different, the slip system parameters are also different. Usually, the method followed in the literature [38,42,43] recommends using the stress-strain data from simple tensile tests and calibrating the hardening parameters so that the results from the simulation match the experimental data. The same procedure is followed here.

For single crystals with two different loading orientations, the stress-strain data for aluminium is taken from the literature [46,47]. For the polycrystalline aluminium, standard tensile tests have been carried out in this work, and the stress-strain curve has been evaluated. The stress-strain curve is mainly influenced by four different slip system level hardening parameters, i.e., $h_0, s_s, s_{s0},$ and s^α, as described in Section 4. These four parameters have been calibrated by comparing the results of FE simulation with experimentally obtained stress-strain curves, as presented in Figure 7. It may be noted that the parameter s_{s0} is calibrated by comparing the yield stress of the material (experiment vs. analysis). The initial hardening slope is governed by the parameters h_0. The asymptotic saturation value of the stress-strain curve is influenced by the parameters s_s and s^α.

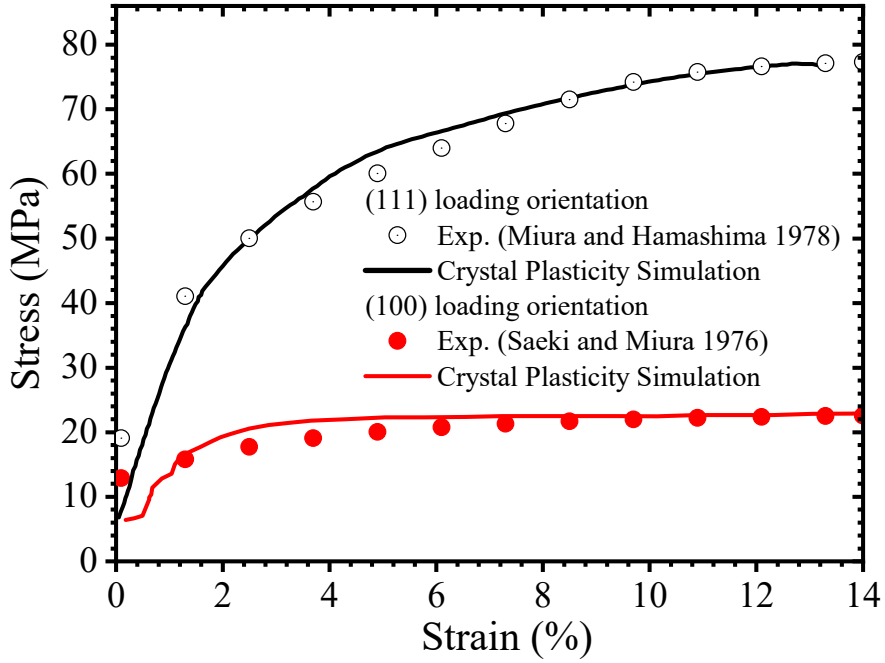

Figure 7. Calibration of parameters of crystal plasticity model for single crystal aluminium for loading along two different orientations (i.e., <111> and <100>) by comparing stress-strain curve from FE simulation with experimental data from the literature [46,47].

By using this approach and varying the parameters systematically, the four parameters are calibrated for both the single crystal as well as the polycrystalline aluminium. The values for the parameters are presented in Table 5 for both the single-crystal orientations and the polycrystal. For polycrystalline aluminium, the comparison of stress-strain curves as obtained from FE analysis and experiment is presented in Figure 8.

The elastic constants are taken from the literature [43]. These parameters have been used later for the simulation of load-displacement behaviour and for the evaluation of critical damage parameters of the disc-type CT specimens of both single-crystal and polycrystalline aluminium.

Table 5. Values of different parameters of the crystal plasticity model used in the FE simulation.

Parameter	<100> Orientation	<111> Orientation	Polycrystalline
Euler angles (in degrees) (ϕ, θ, ϕ')	(0, 0, 0)	(45, 35.26, 0)	Uniform distribution
Initial slip hardening parameter (h_0) in MPa	60	63	65
Saturation slip resistance (s_s) in MPa	11	19.5	25
Initial value of s_s(i.e., s_{s0}) in MPa	1	1	5
Total slip resistance (s^α) in MPa	50	50	65
Elastic constants (C_{11}, C_{12}, C_{44}) in GPa	(112.9, 66.5, 27.8)	(112.9, 66.5, 27.8)	(112.9, 66.5, 27.8)
Poisson's ratio (ν)	0.35	0.35	0.35

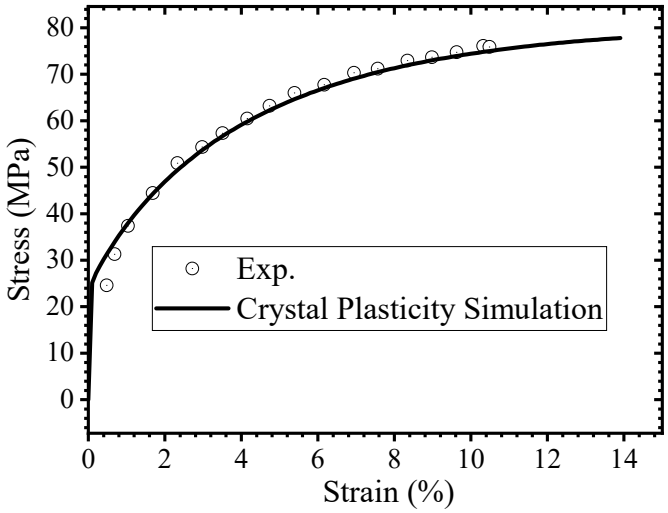

Figure 8. Calibration of parameters of crystal plasticity model for polycrystalline aluminium by comparing stress-strain curve from FE simulation with experiment carried out in this work.

6. Experimental Validation of Results of Crystal Plasticity Simulation and Evaluation of Critical Damage Parameter

In this section, the results of the crystal plasticity simulation of disc-type specimens are presented first, followed by a presentation of the results of Rice and Tracey's damage model [30]. The above damage model has been used to characterise ductile crack initiation in the specimens. The finite element mesh of half of the disc-type CT specimen is presented in Figure 9a, and the zoomed view of the mesh near the crack tip is shown in Figure 9b. The dimensions of the model are provided in Figure 1.

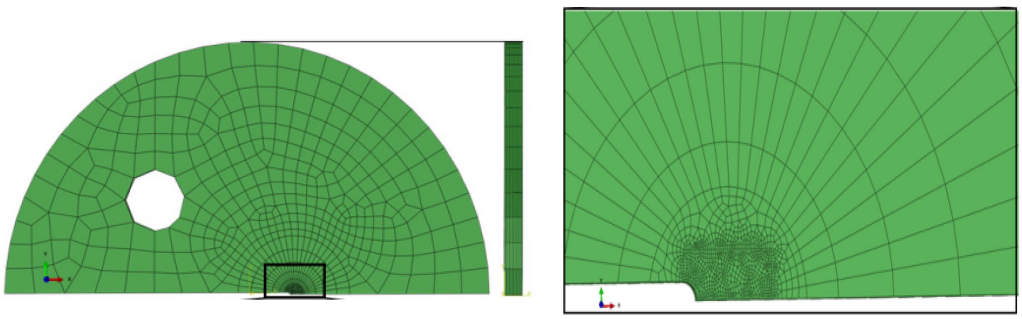

(**a**) (**b**)

Figure 9. (**a**) Front view of the symmetric model of finite element mesh of the disc-shaped compact tension specimen (the side view is shown on the right); (**b**) enlarged view near the crack tip.

Due to symmetry, only half of the specimen is modelled. The bottom surface of the specimen (in the region of the remaining ligament) is fixed in the vertical (i.e., loading) direction; however, the crack face remains free. The loading is applied near the hole so as to simulate the displacement-controlled loading as applied in the experiment. The contour plots of von Mises stress, equivalent plastic strain and hydrostatic pressure (which is negative of hydrostatic stress σ_m) for a given instant of loading (e.g., an applied displacement of 0.35 mm) are presented in Figure 10.

(**a**)

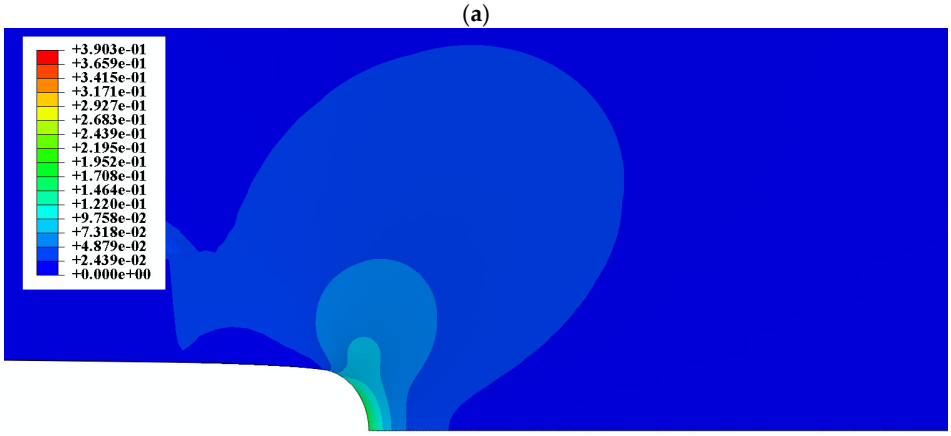

(**b**)

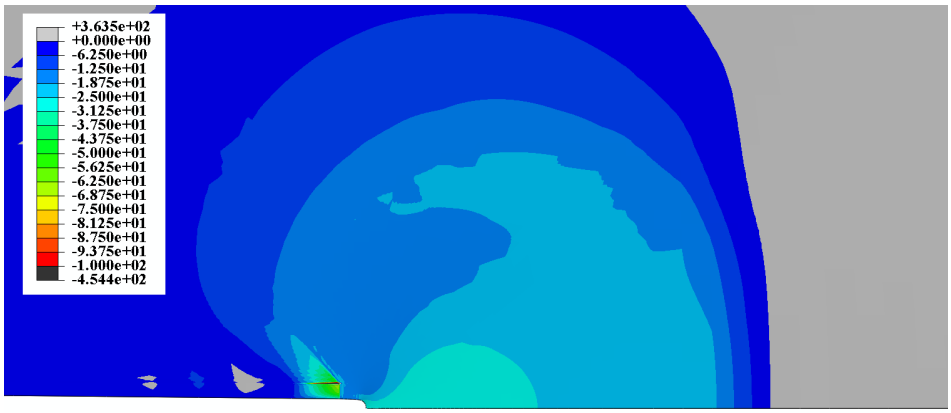

(**c**)

Figure 10. Contour of (**a**) von Mises equivalent stress (in MPa), (**b**) equivalent plastic strain, and (**c**) hydrostatic pressure (in MPa) near the crack tip region of the disc-type CT specimen when loaded by an applied displacement of 0.35 mm.

It can be observed from Figure 10a that the von Mises equivalent stress and the plastic strain are highest near the crack tip, and they decrease with distance from the crack tip. This is due to the stress concentration near the crack tip region and is similar to the typical crack tip stress and strain field of fracture specimens. The hydrostatic stress (negative of pressure) is maximum at a region that is slightly away from the crack tip. As the crack tip deforms plastically, it blunts, and hence, the hydrostatic stress field gets relaxed near the tip due to the presence of a free surface. It peaks at some distance from the crack tip and not exactly at the crack tip. These data of mean hydrostatic stress, along with von Mises equivalent stress and equivalent plastic strain, are used later in the evaluation of damage parameters, as presented in the following paragraphs.

The load-displacement data are calculated from the results of crystal plasticity simulations using the model parameters, as presented in Table 5. The results of the simulation are presented in Figure 11, along with experimental data for the disc-type CT specimens with three different a/W ratios (i.e., 0.4, 0.5, and 0.6). The results of the FE simulation compare very well with those of the experiment, as can be seen from Figure 11, and hence, the model is validated.

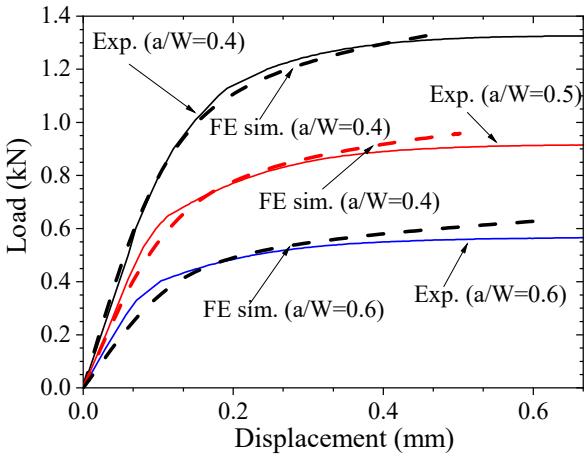

Figure 11. Stress-strain curve of the aluminium alloy as obtained from FE simulation with crystal plasticity model and its comparison with experimental data.

It may be noted that the load-carrying capacity of the specimen with a/W of 0.4 is higher when compared with that of the specimens with a/W ratios of 0.5 and 0.6 as the remaining ligament (which is the load-carrying area) is higher. Once the load-displacement data are validated, our objective is to evaluate a critical damage parameter, which can be used to predict the ductile crack initiation in the specimens and components of this material. The evaluation procedure for Rice and Tracey's damage parameter [30] is presented as follows.

One of the damage models for the prediction of ductile crack initiation in materials is due to Rice and Tracey [30]. This parameter is widely used in the literature, and it is well-known that it is a material constant [37,38]. Hence, this parameter was also used to predict crack initiation in smooth as well as notched tensile specimens (with different values of notch radii) of nuclear-grade carbon steel in ref. [37] In ref. [38], this parameter was used in the crystal plasticity simulation to predict fatigue crack initiation in Ti-6Al-4V alloy. Due to the above advantages of this parameter, we used it for the simulation of ductile crack initiation in aluminium alloy Al-1100. The damage parameter D is defined as the following [30]:

$$D = A \int_0^{\varepsilon_f} \exp\left(1.5\frac{\sigma_m}{\sigma_{eq}}\right) d\varepsilon_{eq}^p \tag{13}$$

In Equation (13), A is a constant whose value is 0.283 as per ref. [30], σ_m is the mean hydrostatic stress, σ_{eq} is the von Mises equivalent stress, and ε_{eq}^p is the von Mises equivalent

plastic strain. From the FE simulation, the values of all the above three parameters are known for each step of loading and at each integration point of the FE mesh. These are integrated using Equation (13) till a given value of applied displacement. The values of applied displacements at crack initiation for various types of disc CT specimens are obtained from the experiment, and these are presented in Figure 12, along with load-displacement data.

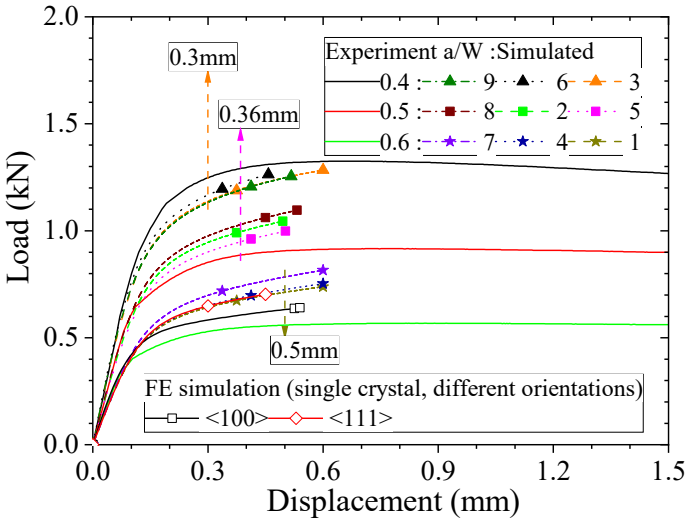

Figure 12. Identification of ductile crack initiation in experimental load-displacement curves of disc-type CT specimens with various a/W ratios and the corresponding results of crystal plasticity simulation.

It can be observed from Figure 12 that the values of applied displacements at crack initiation are 0.3, 0.36, and 0.5 mm for the specimens with a/W ratios of 0.4, 0.5, and 0.6, respectively. It may be noted that crack initiation occurs at a lower value of applied displacement for the specimens with a lower a/W ratio as the crack length is smaller. A smaller value of crack length means the remaining ligament 'b' is larger, as the total width W is the same for all the specimens. For the specimens with a larger remaining ligament, the stiffness is higher, and hence, the crack tip constraint is higher when compared with specimens with lower values for the remaining ligament. Hence, the crack initiation occurs for a lower value of applied displacement for specimens with lower a/W ratios.

Using the data of stress and plastic strain fields from FE analysis, the damage parameter is evaluated using Equation (13), and this parameter keeps on increasing with increasing value of applied displacement due to the process of integration of the incremental damage function. The critical damage parameter is evaluated corresponding to the applied displacement, which coincides with ductile crack initiation as observed in the experiments (these values are already presented earlier). The variation of damage parameter as a function of distance from the crack tip for the disc-type CT specimen and other results are presented in the next section.

7. Results and Discussion

The material damage factor D is calculated from stress and plastic strain fields ahead of the crack tip using Equation (13), and its variation with distance from the crack tip is plotted in Figure 13. The data are presented for various values of applied displacements ranging from 0.1 to 0.36 mm. As we move away from the crack tip, the stress and plastic strain fields decay (as can be seen from the contour plots of Figure 10), and hence, a similar trend is also observed for the material damage parameter, which has a maximum value at the crack tip.

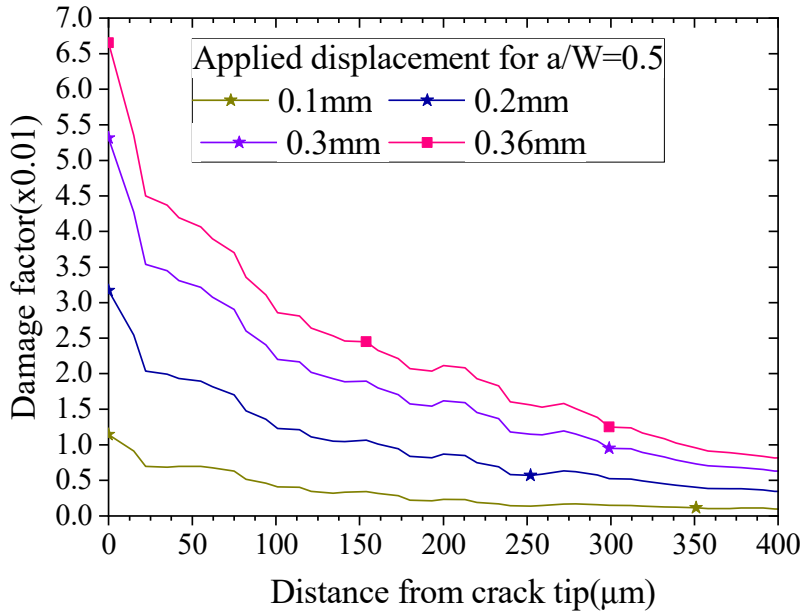

Figure 13. Variation of material damage parameter as a function of distance from crack tip and its evolution for various values of applied displacements for the specimen with a/W ratio of 0.5.

The crack initiation in the specimen occurs when this material damage parameter reaches a critical value, as per the literature [30,37,38]. The critical value of Rice and Tracey's damage parameter, i.e., D_c, is obtained from the results of FE simulations and these are plotted for all nine different specimens in Figure 14 and listed in Table 6. As can be seen from Figure 14, specimens 1 and 4 are outliers, and hence, these are not considered further. For the rest of the 7 specimens, the average value of D_c is 0.065. The deviation of the critical damage parameter of each specimen from the average value is very small, and hence, the average value of 0.065 can be considered as the critical damage factor D_c, signifying ductile crack initiation in the aluminium alloy considered in this work.

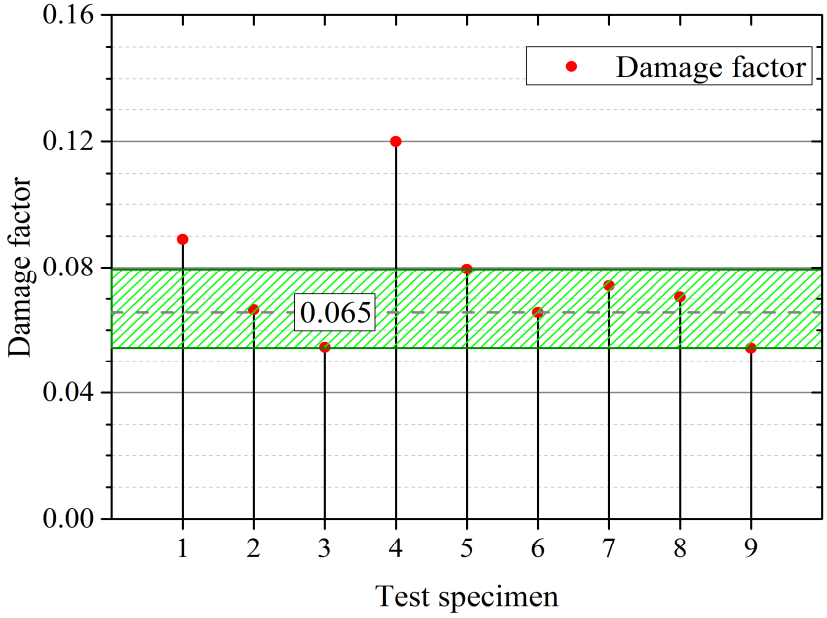

Figure 14. Variation of critical value of material damage parameter signifying crack initiation in specimens with different a/W ratios for the nine different disc-type CT specimens. The green area is the zone of experimental scatter.

Table 6. Comparison of damage factors for different types of disc-shaped CT specimens.

Nominal a/W	Test No.	Damage Factor Value at Crack Initiation D_c	Average of D_c	% Deviation from Average Value
0.6	1	0.904	0.065 (excluding outliers 1 and 4)	-
	4	0.124		-
	7	0.074		12
0.5	2	0.066		1.5
	5	0.079		17
	8	0.07		7.1
0.4	3	0.066		1.5
	6	0.055		18
	9	0.055		18

The effect of crystal orientation on the fracture initiation toughness of aluminium single crystals has now been studied using this critical damage parameter D_c. Using the crystal plasticity material model, two different kinds of orientations are analysed, i.e., crack along the [100] and [111] planes. The specimen geometry is the same as that presented in Figure 1, and the FE mesh is the same as shown in Figure 9. The a/W ratio of the specimen is taken as 0.6 and the loading direction is perpendicular to the crack plane. The loading directions are also denoted as <100> and <111> for the two cases considered in this work. The results of variation of damage parameter ahead of the crack tip as a function of distance from the crack tip are presented in Figure 15 for the two orientations as mentioned above.

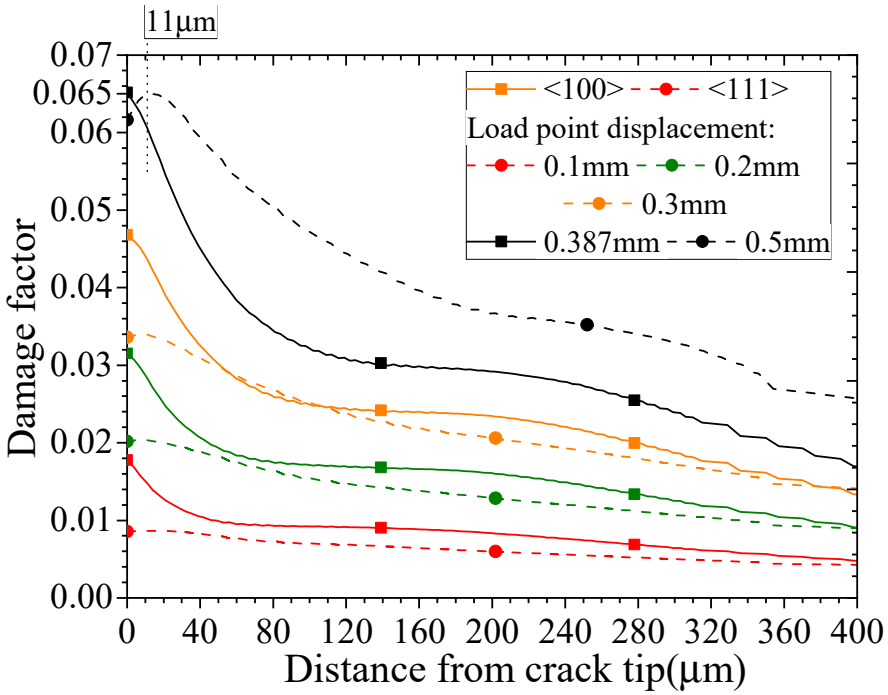

Figure 15. Variation of damage factor as a function of distance from crack tip for single crystal fracture specimens for two different crystal orientations and for various levels of applied displacement loading (dotted line for results of <111> loading direction and solid line for results of <100> loading direction).

As the applied displacement is increased, the damage parameter at a fixed point along the ligament increases and it decreases with distance as one moves away from the crack tip. It can be observed that the damage parameter for both crystal orientations attains a

critical value of 0.065 for an applied displacement of 0.5 mm, which is very similar to that of polycrystalline experimental data, as presented in Figure 12. The data for the <100> loading direction are marked with solid lines, whereas those for the <111> loading direction are marked with dotted lines. As can be seen from Figure 15, the values of the damage parameter for the <111> loading direction are higher all throughout the ligament compared with that of the <100> loading direction when the displacement values approach 0.5 mm (which is close to that of ductile crack initiation in the specimens).

However, for lower displacements (i.e., 0.1 and 0.2 mm), the damage values across the ligament are smaller for the <111> orientation. This can be explained from the point of view of crack tip constraint for the two specimen orientations. The [111] plane is a closed pack plane (whereas [100] is not closely packed) in face-centred cubic crystals (such as aluminium), and hence, the crystals are easy to slip by shear in the [111] plane; however, they are difficult to open by tension. This leads to lower values of plastic deformation and, hence, lower damage parameters, initially during the deformation process. However, as one increases the applied loading, the resolved shear stresses in the [111] plane increase and when the resolved shear stress exceeds the critical value, the [111] plane slips easily by shear, and there is a sudden onset of large plastic deformation around the crack tip. This can be seen from the nature of the damage parameter curve, as presented in Figure 15.

It may be noted that the damage parameter values peak at a distance of 11 microns from the crack tip (and not exactly at the crack tip) in the case of <111> loading direction. This can be explained with the help of the process of crack tip blunting due to large shear-type plastic deformation of the crack tip for the <111> loading direction. As the crack tip blunts, a free surface is created, and hence, the hydrostatic stress reduces near the crack tip. It peaks slightly away from the crack tip (i.e., it is not at maximum at the crack tip). Such kinds of observations have also been presented earlier in the literature [33–35].

It can be seen from Equation (13) that the damage parameter is an exponential function of hydrostatic stress. Hence, as the hydrostatic stress near the crack tip relaxes due to excessive plastic deformation for the <111> loading direction, the damage near the crack tip also becomes slightly lower. It peaks at a distance from the crack tip, as can be seen in Figure 15. Again, the damage values for the <111> loading direction are also larger across the ligament when compared with that of <100> loading direction for applied displacement values of 0.5 mm and more. Hence, it can be concluded that the specimen with [111] crack plane and <111> loading direction is more prone to ductile crack growth (hence, has lower crack initiation and propagation toughness) when compared with that of the specimen with [100] crack plane and <100> loading direction. This information can be used further in order to tailor the texture of alloys so as to increase the fracture toughness property.

8. Conclusions

In this work, experiments have been conducted on disc-shaped compact tension specimens machined from an aluminium alloy Al-1100-O block, which is usually used for the manufacture of the fuel clad components of research-type nuclear reactors. To study ductile crack initiation in this material, a material damage parameter based on Rice and Tracey's model has been evaluated from the results of crystal plasticity-based FE simulations. The critical value of Rice and Tracey's damage parameter has been evaluated from combined crystal plasticity simulation and experimental data regarding applied displacement at crack initiation. The following conclusions can be obtained from this study.

- With increasing a/W ratio, the load-bearing capacity of the disc-shaped specimen becomes lower for a given value of applied displacement as the remaining ligament decreases with increasing a/W ratio.
- The fracture resistance curve for Al-1100-O was seen to be almost independent of the a/W ratio of the fracture specimens (for a/W values in the range of 0.4 to 0.6).
- The critical damage parameters, as evaluated from crack tip stress and strain fields of crystal plasticity-based FE simulation results for nine different specimens, have a small range when the results of two outliers are discarded.

- The mean value of critical damage parameter D_c was determined to be 0.065 for this material.
- The crystal with <111> loading direction is more prone to crack initiation (hence, has lower crack initiation and propagation toughness) when compared with that of the crystal with <100> loading direction. This can be explained on the basis of the onset of large-scale plastic deformation in the [111] planes once the resolved shear stress exceeds the critical value for slip to occur. Hence, the damage parameters are higher for <111> loading direction when compared with those of <100> loading direction only at larger displacement values of 0.5 mm and more.

Author Contributions: Conceptualisation, M.K.S.; methodology, M.K.S., T.S. and A.S.; software, T.S.; validation, M.K.S., T.S. and A.S.; formal analysis, M.K.S., T.S. and A.S.; investigation, M.K.S. and A.S.; resources, M.K.S.; data curation, M.K.S. and T.S.; writing—original draft preparation, M.K.S. and T.S.; writing—review and editing, M.K.S., T.S. and A.S.; visualisation, M.K.S. and T.S.; supervision, M.K.S.; project administration, M.K.S.; funding acquisition, M.K.S. All authors have read and agreed to the published version of the manuscript.

Funding: This research received no external funding.

Institutional Review Board Statement: Not Applicable.

Informed Consent Statement: Not Applicable.

Data Availability Statement: The data presented in this study are available on request from the corresponding author. The data are not publicly available due to privacy.

Acknowledgments: The authors acknowledge the head of the Reactor Safety Division, BARC Mumbai, for his constant encouragement for this research.

Conflicts of Interest: The authors declare no conflicts of interest.

References

1. Hicks, J. *Welded Joint Design*, 3rd ed.; Woodhead Publishing: Sawston, UK, 1999.
2. Xu, S.; Deng, X. Nanoscale void nucleation and growth and crack tip stress evolution ahead of a growing crack in a single crystal. *Nanotechnology* **2008**, *19*, 115705. [CrossRef]
3. Liu, T.; Groh, S. Atomistic modelling of the crack–void interaction in α Fe. *Mater. Sci. Eng. A* **2014**, *609*, 255–265. [CrossRef]
4. Balakrishnan, V.; Roshan, P.; Goel, S.; Jayaganthan, R.; Singh, I.V. Experimental and XFEM simulation of tensile and fracture behaviour of Al 6061 alloy processed by severe plastic deformation. *Metallogr. Microstruct. Anal.* **2017**, *6*, 55–72. [CrossRef]
5. Gairola, S.; Jayaganthan, R. XFEM simulation of tensile and fracture behaviour of ultrafine-grained Al 6061 alloy. *Metals* **2021**, *11*, 1761. [CrossRef]
6. Das, P.; Singh, I.V.; Jayaganthan, R. Crack growth simulation of bulk and ultrafine grained 7075 Al alloy by XFEM. *Int. J. Mater. Prod. Technol.* **2012**, *44*, 252–276. [CrossRef]
7. Kang, B.S.J.; Kobayashi, A.S.; Post, D. Stable crack growth in aluminum tensile specimens. *Exp. Mech.* **1987**, *27*, 234–245. [CrossRef]
8. Hellier, A.K.; Chaphalkar, P.P.; Prusty, B.G. Fracture toughness measurement for aluminium 6061-T6 using notched round bars. In Proceedings of the 9th Australasian Congress on Applied Mechanics 2017 (ACAM 9), Sydney, Australia, 27–29 November 2017.
9. Gairola, S.; Joshi, A.; Gangil, B.; Rawat, P.; Verma, R. Correlation of Tensile Properties and Fracture Toughness with Microstructural Features for Al–Li 8090 Alloy Processed by Cryorolling and Post-rolled Annealing. *Trans. Indian Inst. Met.* **2019**, *72*, 1743–1755. [CrossRef]
10. Rahmatabadi, D.; Hashemi, R.; Mohammadi, B.; Shojaee, T. Experimental evaluation of the plane stress fracture toughness for ultra-fine grained aluminum specimens prepared by accumulative roll bonding process. *Mater. Sci. Eng. A* **2017**, *708*, 301–310. [CrossRef]
11. Gattu, M.; Aala, S. Size-effect method to determine mode-I fracture toughness of aluminium alloys. *Eng. Fract. Mech.* **2021**, *242*, 107504. [CrossRef]
12. Kang, B.S.J.; Kobayashi, A.S. J-resistance curves in aluminum SENT specimens using Moiré interferometry. *Exp Mech* **1988**, *28*, 154–158. [CrossRef]
13. MacMaster, F.J.; Chan, K.S.; Bergsma, S.C.; Kassner, M.E. Aluminum alloy 6069 part II: Fracture toughness of 6061-T6 and 6069-T6. *Mater. Sci. Eng. A* **2000**, *289*, 54–59. [CrossRef]
14. Wang, W.; Jia, L.; Ma, Y. Effect of retrogression temperature on the fracture toughness of 7136 aluminum alloy. *Mater. Chem. Phys.* **2023**, *294*, 126954. [CrossRef]
15. Tsangarakis, N. All modes fracture toughness of two aluminium alloys. *Eng. Fract. Mech.* **1987**, *26*, 313–321. [CrossRef]

16. Ye, T.; Xia, E.; Qiu, S.; Liu, J.; Yue, H.; Tang, J.; Wu, Y. Deformation behaviour of an extruded 7075 aluminum alloy at elevated temperatures. *Materials* **2024**, *17*, 1210. [CrossRef]
17. Zhu, S.; Zhao, M.; Mao, M.; Liang, S.Y. Study on hot deformation behaviour and texture evolution of aluminum alloy 7075 based on visco-plastic self-consistent model. *Metals* **2022**, *12*, 1648. [CrossRef]
18. Pavel, A.S.; Eugene, S.S.; Yuliya, V.M.; Kirill, V.N.; Alexey, I.S.; Dmitry, K.R.; Alexander, M.K. On the grain microstructure–mechanical properties relationships in aluminium alloy parts fabricated by laser powder bed fusion. *Metals* **2021**, *11*, 1175. [CrossRef]
19. Meng, Y.; Wang, X.; Zongcheng, H.; Fu, X. The influence of forming directions and strain rate on dynamic shear properties of aerial aluminum alloy. *Appl. Sci.* **2018**, *8*, 520. [CrossRef]
20. Gilbert, K.J. *Fracture Resistance of Aluminum Alloys: Notch Toughness, Tear Resistance and Fracture Toughness*; ASM International: Materials Park, OH, USA, 2001.
21. Bucci, R.J. Selecting aluminum alloys to resist failure by fracture mechanisms. *Eng. Fract. Mech.* **1979**, *12*, 407–441. [CrossRef]
22. Wang, D.; Zhang, W.; Yi, Y.; Huang, S.; He, H.; Tong, D.; Guo, W. Investigation on strength, toughness and microstructure of cryogenically-deformed 7A85 aluminum alloy under various aging tempers. *Mater. Charact.* **2022**, *193*, 112324. [CrossRef]
23. Wang, D.; Zhang, W.; Huang, S.; Yi, Y.; He, H. Effect of three-dimensional deformation at different temperatures on microstructure, strength, fracture toughness and corrosion resistance of 7A85 aluminum alloy. *J. Alloys Compd.* **2022**, *928*, 167200. [CrossRef]
24. Jiang, L.; Fu, H.; Zhang, Z.; Zhang, H.; Zhang, X.; Feng, X.; Xu, X.; Mao, M.; Xie, J. Synchronously enhancing the strength, toughness, and stress corrosion resistance of high-end aluminum alloys via interpretable machine learning. *Acta Mater.* **2024**, *270*, 119873. [CrossRef]
25. Samanta, A.; Lall, A.; Das, H.; Seffens, R.J.; Grant, G.J.; Jana, S. Enhanced toughness and tear resistance of thin-walled high-pressure die-cast aluminum alloys through friction stir processing. *Mater. Lett.* **2024**, *357*, 135752. [CrossRef]
26. Sivaraj, P.; Seeman, M.; Seetharaman, R.; Balasubramanian, V. Fracture toughness properties and characteristics of Friction stir welded high strength aluminium alloy by post weld heat treatment (PWHT). *Mater. Today Proc.* **2021**, *43*, 2150–2155. [CrossRef]
27. Djili, A.; Bezzazi, B.; Zioui, N.; Haboussi, M. Effect of natural aging on the tensile properties and the toughness of friction stir welds of 2024-T3 aluminum alloy. *J. Adv. Join. Process.* **2023**, *8*, 100153. [CrossRef]
28. Abdellah, M.Y. Essential work of fracture assessment for thin aluminium strips using finite element analysis. *Eng. Fract. Mech.* **2017**, *179*, 190–202. [CrossRef]
29. Vishnu, O.S.; Gattu, M. Cohesive zone modelling of thin aluminium sheets. *Mater. Today Proc.* **2020**, *33*, 5672–5677. [CrossRef]
30. Rice, J.; Tracey, D. On the ductile enlargement of voids in triaxial stress fields. *J. Mech. Phys. Solids* **1969**, *17*, 201–217. [CrossRef]
31. Rice, J.R. Tensile crack tip fields in elastic ideally plastic crystals. *Mech. Mater.* **1987**, *6*, 317–335. [CrossRef]
32. Chandra, S.; Samal, M.K.; Kumar, N.N.; Chavan, V.M.; Raghunathan, S. An atomistic modelling and statistical analysis study of crack–void interaction in Aluminum. *Philos. Mag. Lett.* **2017**, *97*, 504–514. [CrossRef]
33. Patil, S.D.; Narasimhan, R.; Mishra, R. A numerical study of crack tip constraint in ductile single crystals. *J. Mech. Phys. Solids* **2008**, *56*, 2265–2286. [CrossRef]
34. Patil, S.; Narasimhan, R.; Biswas, P.; Mishra, K.R. Crack tip fields in a single edge notched aluminum single crystal specimen. *ASME J. Eng. Mater. Technol.* **2008**, *130*, 021013. [CrossRef]
35. Biswas, P.; Narasimhan, R.; Tewari, A. Influence of crack tip constraint on void growth in ductile FCC single crystals. *Mater. Sci. Eng. A* **2011**, *528*, 823–831. [CrossRef]
36. Biswas, P.; Narasimhan, R.; Kumar, A. Interaction between a notch and cylindrical voids in aluminum single crystals: Experimental observations and numerical simulations. *J. Mech. Phys. Solids* **2013**, *61*, 1027–1046. [CrossRef]
37. Samal, M.K.; Dutta, B.K.; Kushwaha, H.S. A study on ductile fracture initiation in the PHT piping material of an Indian PHWR using local approach. *Int. J. Press. Vessel. Pip.* **1999**, *76*, 319–330. [CrossRef]
38. Anahid, M.; Samal, M.K.; Ghosh, S. Dwell fatigue crack nucleation model based on crystal plasticity finite element simulations of polycrystalline titanium alloys. *J. Mech. Phys. Solids* **2011**, *59*, 2157–2176. [CrossRef]
39. *ASTM Committee E08 ASTM E1820-20b*; Standard Test Method for Measurement of Fracture Toughness. ASTM International: West Conshohocken, PA, USA, 2020.
40. Samal, M.K. Development of a model for simulation of micro-twin and corresponding asymmetry in high temperature deformation behavior of nickel-based superalloy single crystals using crystal plasticity-based framework. *Proc. Inst. Mech. Eng. Part C J. Mech. Eng. Sci.* **2017**, *231*, 2621–2635. [CrossRef]
41. Samal, M.K. Simulation of material stress-strain curve and creep deformation response of nickel based superalloys using crystal plasticity based finite element models. *Trans. Indian Inst. Met.* **2016**, *69*, 949–960. [CrossRef]
42. Balasubramanian, S.; Anand, L. Elasto-viscoplastic constitutive equations for polycrystalline FCC materials at low homologous temperatures. *J. Mech. Phys. Solids* **2002**, *50*, 101–126. [CrossRef]
43. Ma, A.; Roters, F. A constitutive model for FCC single crystals based on dislocation densities and its application to uniaxial compression of aluminium single crystals. *Acta Mater.* **2004**, *52*, 3603–3612. [CrossRef]
44. Samal, M.K.; Ghosh, S. Evaluation of creep deformation and mechanical properties of nickel-based superalloys through FE analysis based on crystal plasticity models. *Procedia Eng.* **2013**, *55*, 342–347. [CrossRef]
45. Samal, M.K. Numerical simulation of high temperature deformation behaviour of Nickel-based superalloys using crystal plasticity models and finite element method. *Math. Concepts Appl. Mech. Eng. Mechatron.* **2016**, 414–446.

46. Saeki, Y.; Miura, S. Plastic deformation and prominent cross slip of <100> oriented aluminum single crystals. *J. Soc. Mater. Sci. Jpn.* **1976**, *25*, 710–716.
47. Miura, S.; Hamashima, K. Plastic deformation of <111> oriented aluminum single crystals. *J. Soc. Mater. Sci. Jpn.* **1978**, *27*, 1146–1151.